Electronic Supplementary Information

Molecular Integration of Lewis Bases for Efficient and Stable Inverted Perovskite Solar Cells

Yinhua Lv, [a] *Chi Yang,* [b*] *Zhenhuang Su,* [c] *Tianwei He,* [a] *Ruohao Wang,* [a] *Ruihao Chen,* [*d] *Xingyu Gao*[*c] and Wen-Hua Zhang* [*a]

[a] Yunnan Key Laboratory of Carbon Neutrality and Green Low-carbon Technologies, Yunnan Key Laboratory for Micro/Nano Materials & Technology, Southwest United Graduate School, School of Materials and Energy, Yunnan University, Kunming 650504, China. Email: wenhuazhang@ynu.edu.cn

[b] Key Laboratory of Novel Photovoltaic Materials and Thin Film Solar Cells of Yunnan Provincial, School of Energy and Environment Science, Yunnan Normal University, Kunming, 650500, China. Email: 230019@ynnu.edu.cn

[c] Shanghai Synchrotron Radiation Facility (SSRF), Shanghai Advanced Research Institute, Chinese Academy of Sciences, 239 Zhangheng Road, Shanghai, 201204, China. Email: gaoxy@sari.ac.cn

[d] Department State Key Laboratory of Solidification Processing, Center for Nano Energy Materials, School of Materials Science and Engineering, Northwestern Polytechnical University, Xi'an, 710071, China. Email: rhchen@nwpu.edu.cn

Experimental Section

Materials

All chemicals were used as received without further purification. Rubidium iodide (RbI, 99.99%), cesium iodide (CsI, 99.99%), dimethylformamide (DMF, 99.8%, anhydrous), dimethyl sulfoxide (DMSO, ≥99.9%, anhydrous), isopropanol (IPA, 99.5%), ethanol (99.5%), and anisole (99%) were purchased from Sigma-Aldrich. Anisole (99.7%, anhydrous) was purchased from Aladdin. Lead iodide (PbI_2, 99.99%) was purchased from Advanced Election Technology Co. Ltd. Formamidinium iodide (FAI, 99.9%) and methylammounium bromide (MABr, ≥99.5%) were purchased from Greatcell Solar Materials (Australia). Phenyl-C61-butyric acid methyl-ester ($PC_{61}BM$, 99%), 2,9-Dimethyl-4,7-diphenyl-1,10-phenanthroline (BCP, 99.5%), phenethylammonium iodide (PEAI, 99.5%), and lead bromide ($PbBr_2$, 99.5%) were purchased from Xi'an Yuri Solar Co. Ltd. ([2-(3,6-dimethoxy-9Hcarbazol-9-yl)ethyl]phosphonic acid) (MeO-2PACz, >98%) and trimethyl phosphate (TP, >98.0%) were purchased from Tokyo Chemical Industry (TCI). Dimethyl acetonylphosphonate (DMAPA, 95%) was purchased from Macklin.

Device Fabrication

Perovskite solar cells were fabricated on cleaned and patterned ITO glass substrates (SuZhou ShangYang Solar Technology Co. Ltd.). The ITO substrates were treated by ultraviolet-ozone (UVO) for 15 min before being transformed into the N_2-filled glovebox. The glove box environment was controlled to maintain oxygen levels below 0.1 ppm and relative humidity (RH) below 1%, with temperature maintained at 22 ± 2 °C. The diluted IPA solution of MeO-2PACz (0.5 mg/mL) was spin-coated on the ITO substrate at 3000 rpm for 30 s, followed by annealing at 100 °C for 10 min. The perovskite precursor solution was prepared by mixing CsI (19.5 mg), RbI (15.9 mg), MABr (8.4 mg), FAI (219.5 mg), PbI_2 (656.9 mg), and $PbBr_2$ (27.5 mg) in 1 mL of a mixed solvent (DMF: DMSO = 4:1, v/v), which was stirred for 2 h before use. For the ligand-modified target perovskite solution, each ligand was added directly to the precursor. The perovskite solution was filtered with 0.22 μm PTFE filter. The perovskite precursor solution was spin-coated onto the substrate at 1000 rpm for 10 s,

and 3000 rpm for 40 s. 110 μL of anisole antisolvent was dropped on top of the spinning substrates in the remaining 10 s of the second stage. Sequentially, the perovskite film was annealed at 110 °C for 20 min. After the perovskite film was cooled down to room temperature, 1 mg/mL of PEAI solution was deposited via spin-coating at 5000 rpm for 30 s followed by annealing at 100 °C for 5 min. Then, 15 mg/mL of $PC_{61}BM$ in CB solution and 0.5 mg/mL of BCP in IPA solution were sequentially spin-coated at 1500 rpm for 30 s and 6000 rpm for 40 s. Finally, 100 nm of Ag electrode was thermally deposited by evaporation.

Characterizations

The top-view and the cross-sectional SEM images were measured by using a scanning electron microscopy (FEI inspect f50). Grazing-incidence wide-angle X-ray scattering (GIWAXS) measurements were conducted at the BL14B1 beamline of Shanghai Synchrotron Radiation Facility (SSRF). The antisolvent was dripped on the spinning film at 40 seconds, after another 10 seconds, the spinning process was stopped and the in-situ thermal annealing treatment on the wet film was started immediately. Raising the temperature from 25 to 110 °C with a linear temperature ramp of 1 °C/s. The GIWAXS data was collected every 2 second. In-situ UV-vis absorption spectra were characterized with a home-built dynamic spectrometer system in ambient conditions, and all the measurements were performed on ITO substrates. In-situ PL spectra were obtained using an Ocean Optics' spectrometer with 365 nm UV exciter. The in-siu PL signal of the perovskite films was detected by a receiver positioned at a distance of 1 cm from the sample during annealing. The annealing temperature was set at 110 ℃ for both the in-situ UV-vis absorption and in-situ PL measurements. Kelvin probe force microscopy (KPFM) images were obtained using an atomic force microscope (MultiMode 8, Bruker). The depth profile of the perovskite film on the ITO substrate was recorded using ToF-SIMS (Ion-ToF-SIMS 5) with negative polarity. The pulsed primary Bi^+ ion source was operated at 30 keV, 1 pA, and 7.12+E14 lons/cm^2 on a 300*300 μm^2 area to bombard the sample surface to produce secondary ions. The steady PL spectra and time-resolved PL decay measurements were performed using an FLS980 Series of Fluorescence Spectrometers. X-ray diffraction (XRD) patterns were

attained on a Bruker D8 Advance X powder diffraction system using Cu Kα radiation source (λ = 1.54 Å) operating at 40 kV and 40 mA. XPS measurements were performed on a PHI 5000 Versaprobe III X-ray photoelectron spectrometer. The FTIR spectroscopy was measured by Fourier Transform Infrared Spectrometer (IR-2000, Jingtuo Instrument Technology Co. Ltd.). The UV-Vis spectra were measured by Ultraviolet-Visible Spectrometer (UV-2600i, Shimadzu). The TPC, TPV, IMVS, IMPS, EIS, and Mott-Schottky plots were obtained by Fluxim Paios Spectrometer. The obtained impedance spectra were fitted with Z-View 4 software.

The current-density (*J-V*) measurement was performed via the solar simulator (SS-X50, Enlitech) along with AM 1.5G spectra whose intensity was calibrated by the certified standard silicon solar cell (SRC-2020, Enlitech) at 100 mW/cm^2. The *J-V* curves were measured by forward (-0.1 V to 1.2 V forward bias) or reverse (1.2 V to -0.2 V) scans with a voltage step of 20 mV and a delay time of 100 ms for each point. The active area of a PSC is 0.09 cm^2. The *J-V* curves were obtained by masking the cell with a metal mask of 0.09 cm^2 in area. The external quantum efficiency (EQE) data were obtained by using the solar-cell spectral-response measurement system (QE-R, Enlitech).

The unencapsulated devices for long-term stability measurement were stored in a N_2-filled glovebox under dark (temperature is about 25 ^{o}C). After various periods of time, the *J-V* measurements were performed.

The unencapsulated devices for thermal aging evaluation were placed under a 65 ^{o}C hotplate in a N_2-filled glovebox. The chamber atmosphere (RH) is maintained at less than 1%. After various periods of time, the *J-V* curves were collected.

The dynamic MPP tracking of the unencapsulated devices were carried out by a multi-channels solar cells stability test system with an LED light source (6500K, white-light LED array) calibrated to equivalent one sum illumination (Wuhan 91PVKSolar Technology Co. Ltd, China).

Theoretical Calculation

All the calculations are performed in the framework of the density functional theory with the projector augmented plane-wave method, as implemented in the Vienna

ab initio simulation package.[1] The generalized gradient approximation proposed by Perdew-Burke-Ernzerhof (PBE) is selected for the exchange-correlation potential.[2] The cut-off energy for plane wave is set to 480 eV. The energy criterion is set to 10^{-4} eV in the iterative solution of the Kohn-Sham equation. All the structures are relaxed until the residual forces on the atoms have declined to less than 0.05 eV/Å. To avoid interlaminar interactions, a vacuum spacing of 20 Å is applied perpendicular to the slab.

The binding energy E_{bind} is expressed as:

$$E_{Binding} = E_{A+B} - E_A - E_B$$

where E_{A+B} is the total energy of slab A model with B molecule, E_A is the energy of a A slab, and E_B is that for a B molecule.

Here, we define $\Delta\rho = \rho_{A+B} - \rho_A - \rho_B$ as the charge density difference of A+B heterostructure, where ρ_{A+B}, ρ_A, and $\rho_B$are the charge densities of A+B heterostructure, isolated A and B slabs, respectively.

The adsorption energy Eads is expressed as

$$\Delta E_{ads} = E_{A+B} - E_A - E_B$$

where E_{A+B} is the total energy of slab A model with B adsorption, E_A is the energy of a A slab, and E_B is that for a B molecule.

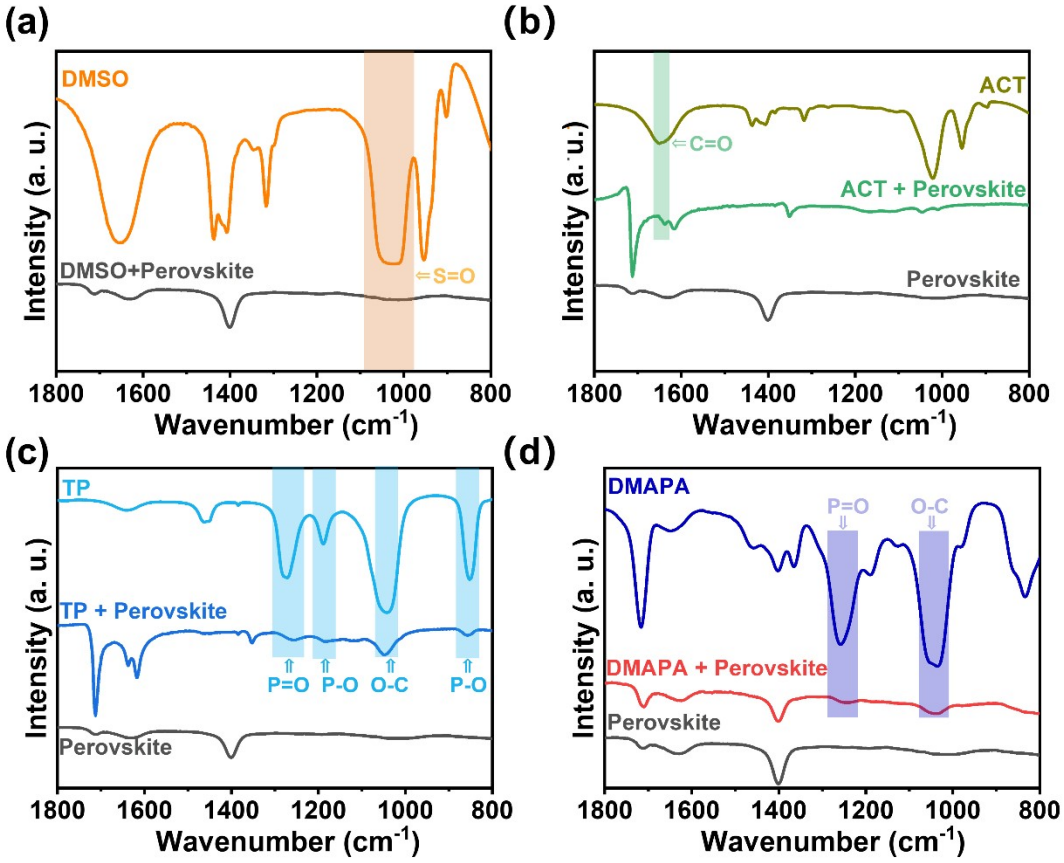

Figure S1. FTIR spectra of pure ligands and the $Rb_{0.05}Cs_{0.05}MA_{0.05}FA_{0.85}Pb(I_{0.95}Br_{0.05})$ perovskite film with ligand modifications: (a) DMSO and the pristine perovskite films; (b) ACT, the pristine perovskite film, and the perovskite with ACT addition; (c) TP, the pristine perovskite film, and the perovskite with TP addition. (d) DMAPA, the pristine perovskite film, and the perovskite with DMAPA addition.

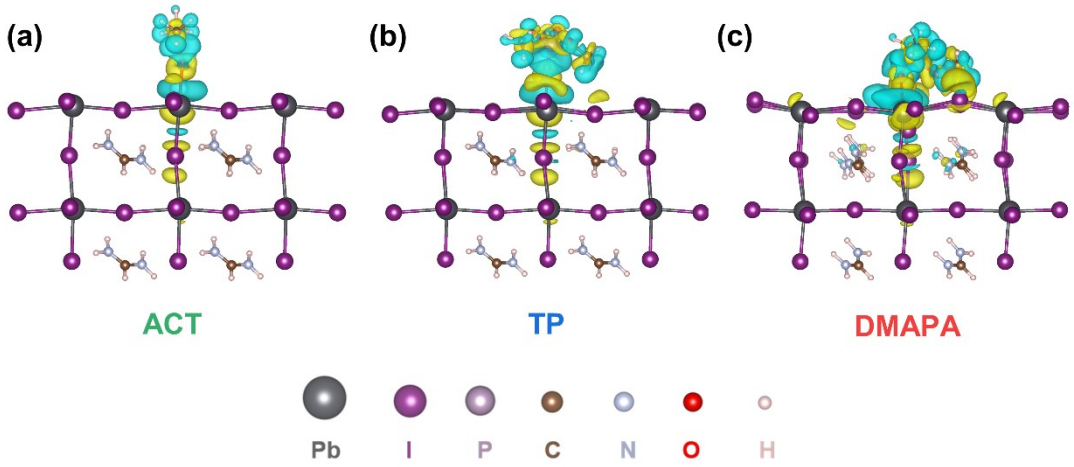

Figure S2. Calculated charge density difference of (a) ACT, (b) TP, and (c) DMAPA ligands onto the $FAPbI_3$ surface with Pb-I termination. The green and yellow represent electron depletion and electron accumulation with the isosurface value of 0.0005 e/Bohr^3, respectively.

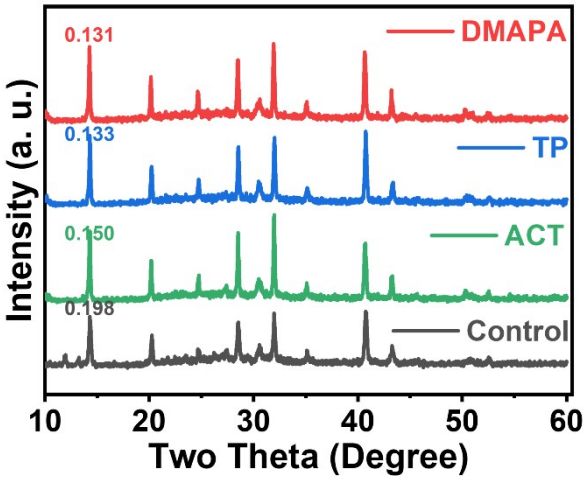

Figure S3. XRD patterns of perovskite films deposited on ITO/MeO-2PACz substrates.

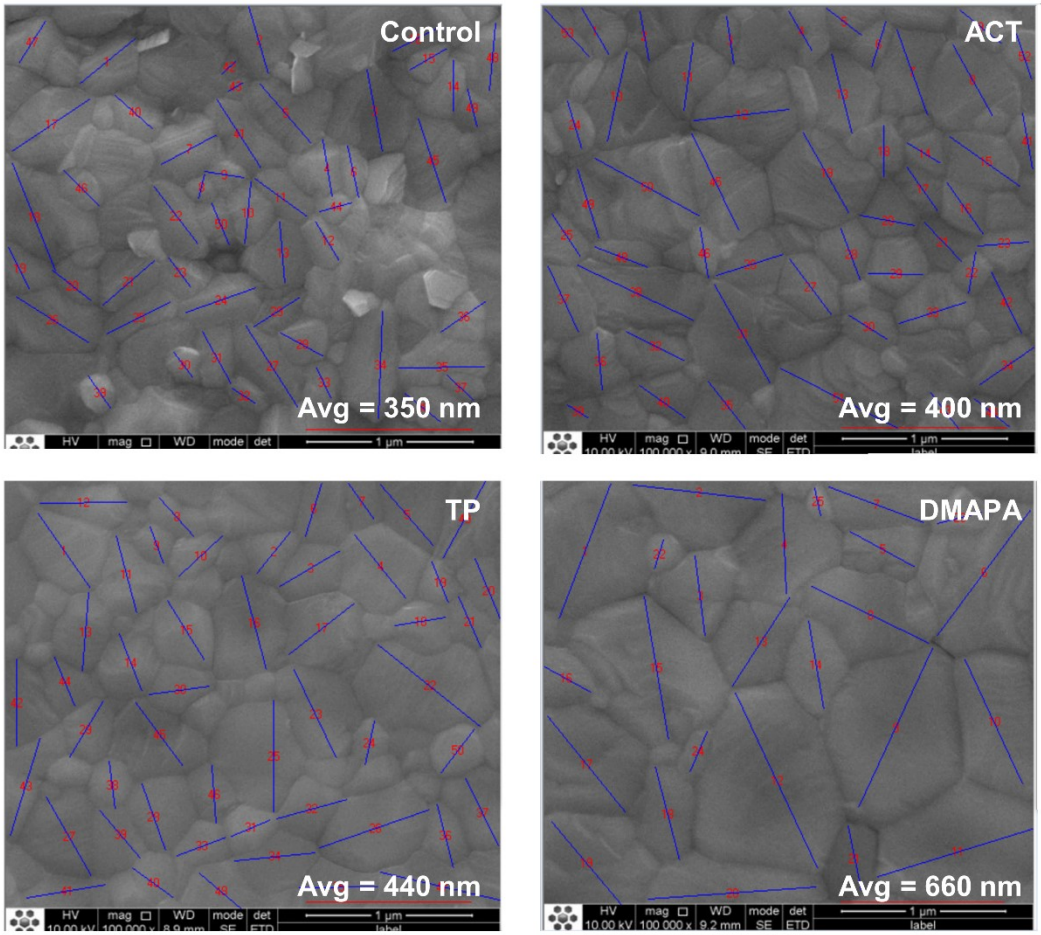

Figure S4. The detailed analysis process of the grain sizes of perovskite films with different ligands.

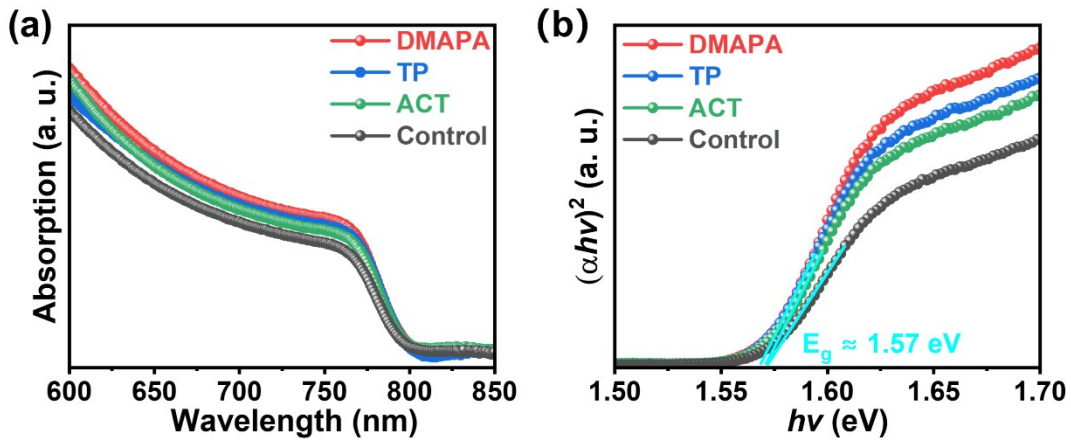

Figure S5. (a) UV-vis absorption plots and (b) the corresponding Tauc plots of the control and treated perovskite films.

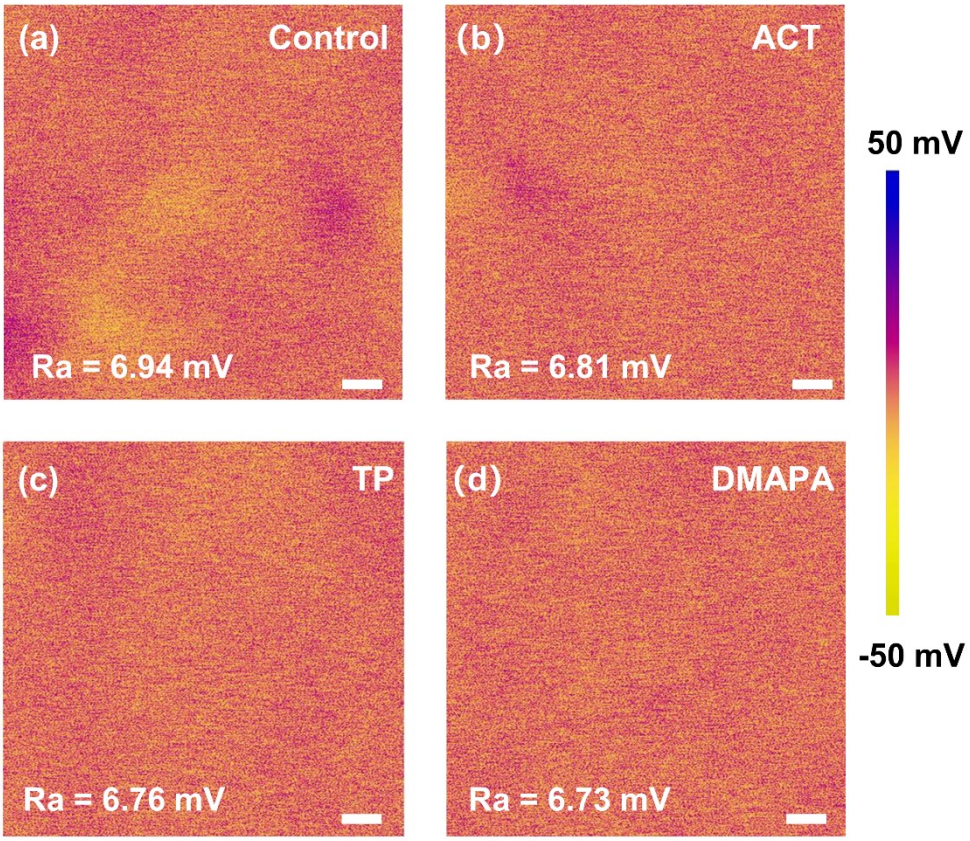

Figure S6. KPFM images of surface potential for (a) the control, (b) ACT-, (c) TP-, and (d) DMAPA-based perovskite films.

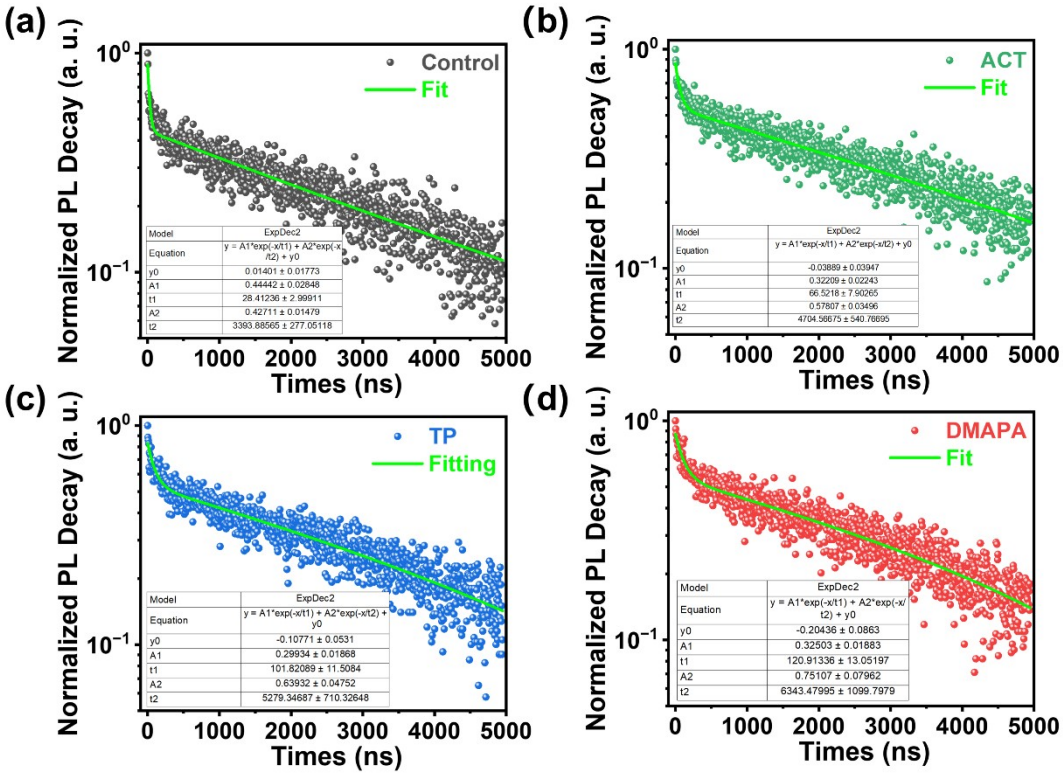

Figure S7. TRPL spectra of the control and treated perovskite films on quartz substrate.

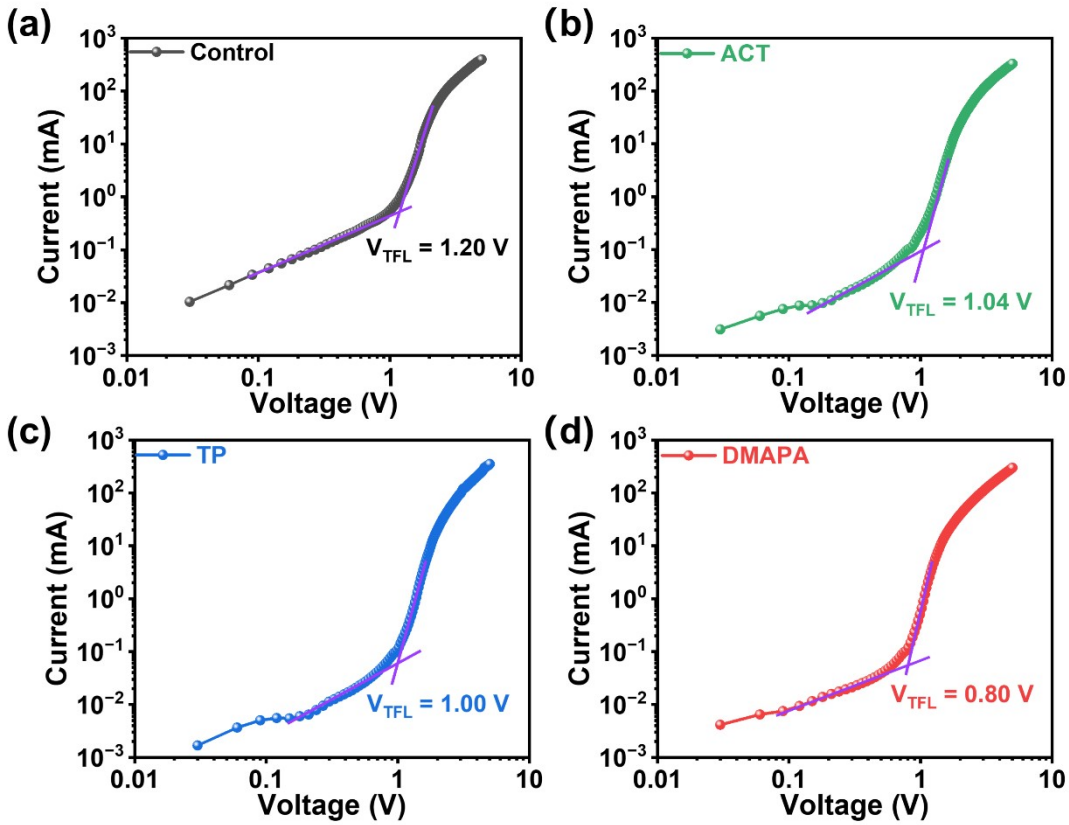

Figure S8. SCLC curves for the electron-only devices based on (a) control, (b) ACT-, (c) TP-, and (d) DMAPA-based perovskite films (employing SnO_2 and PCBM as the bottom and top electron transporting materials).

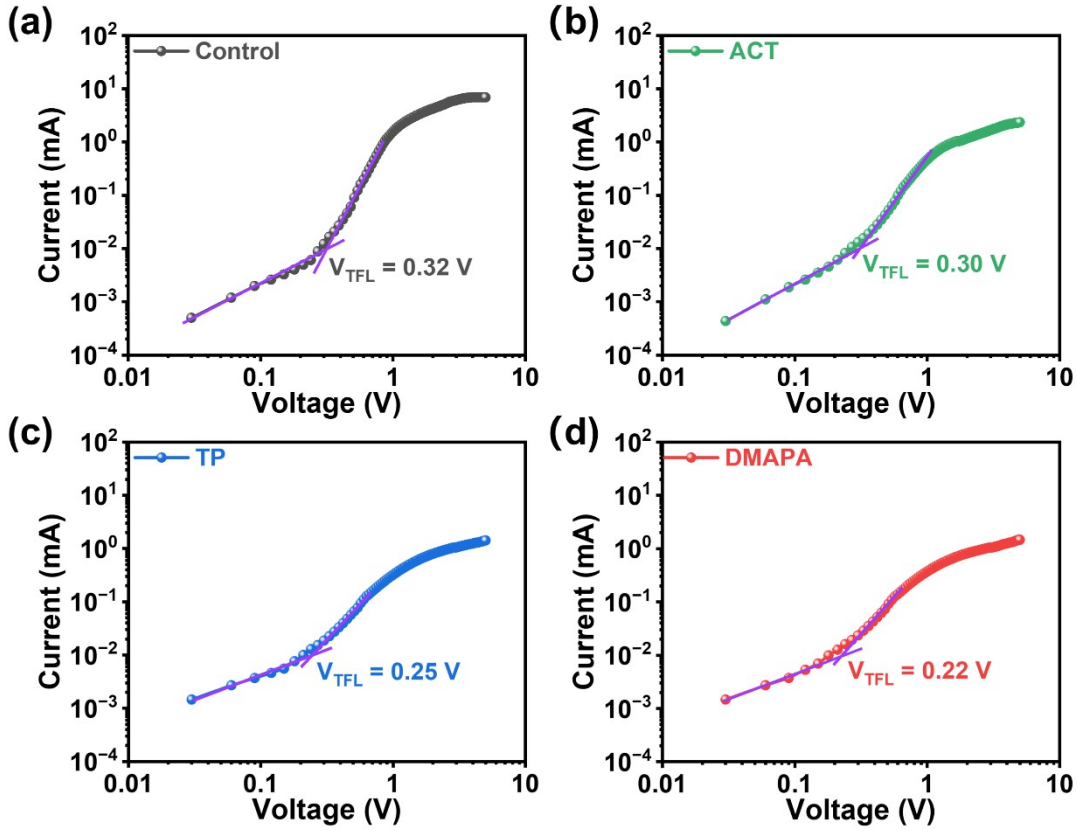

Figure S9. SCLC curves for the control and treated hole-only devices based on of (a) control, (b) ACT-, (c) TP-, and (d)DMAPA-based perovskite films (employing NiO_x and Spiro-OMeTAD as the bottom and top hole transporting materials).

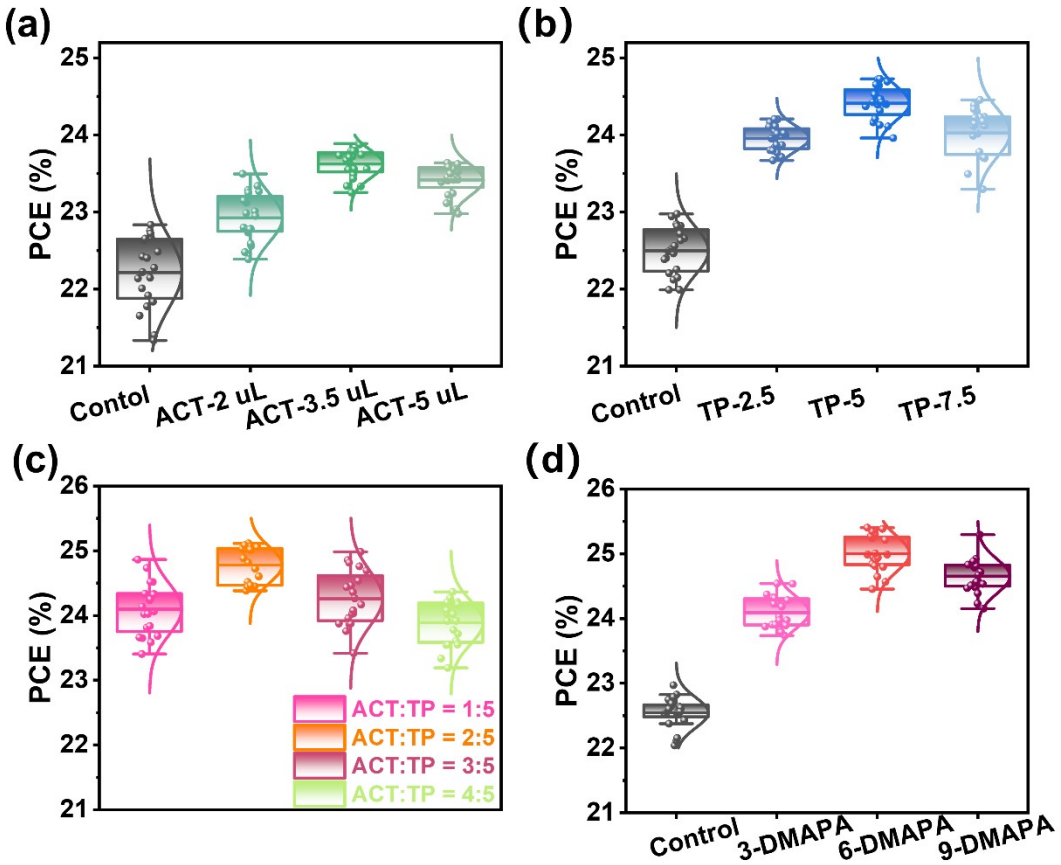

Figure S10. The dependence of PCEs on the concentrations of different ligands: (a) ACT, (b) TP, (c) the ACT + TP, (d) DMAPA.

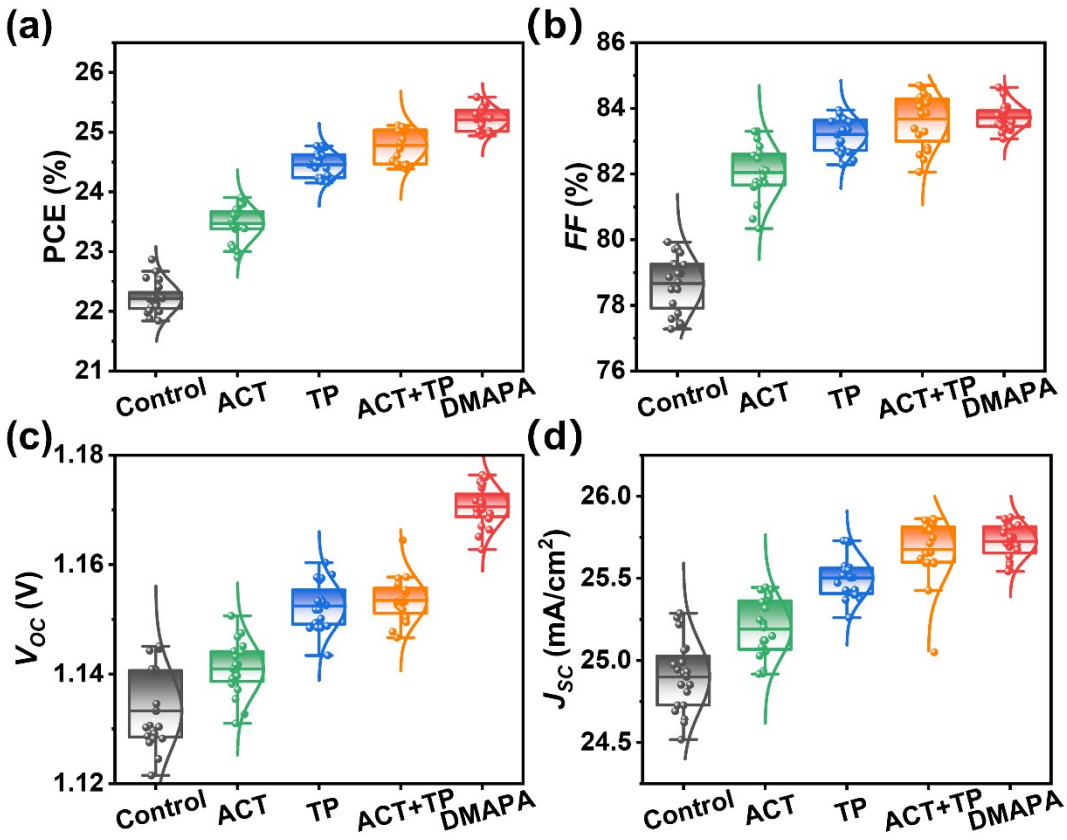

Figure S11. Statistic box plots of *J-V* parameters for devices without and with DMAPA modification for the structure of ITO/perovskite/PCBM/BCP/Ag: (a) PCE, (b) V_{OC}, (c) *FF*, and (d) J_{SC}.

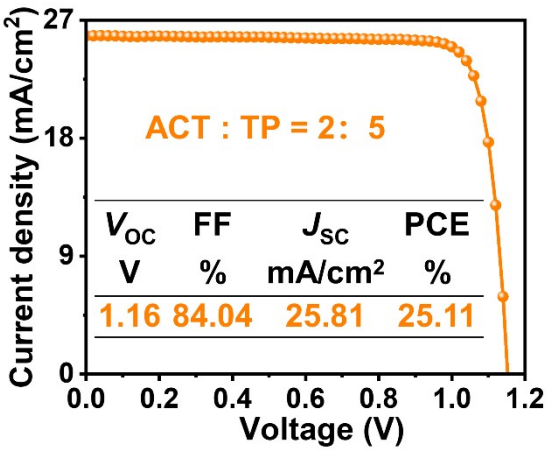

Figure S12. The champion *J-V* curves for the device treated with ACT + TP mixture.

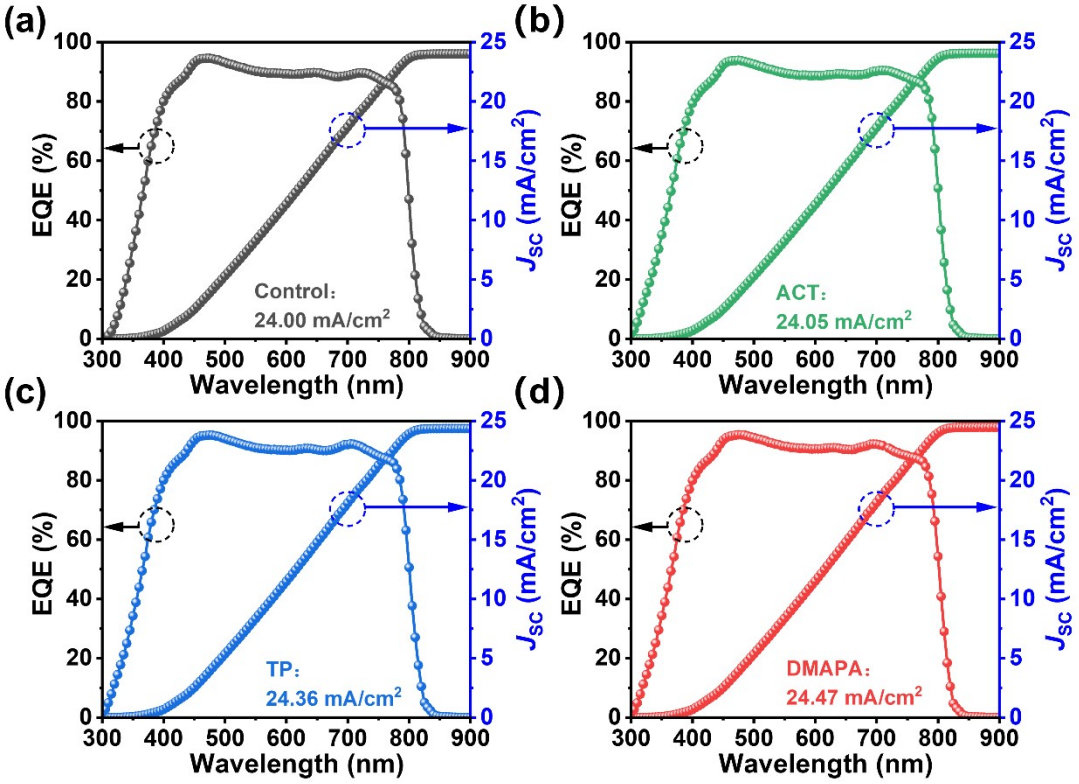

Figure S13. The EQE spectra for (a) control, (b) ACT-, (c) TP-, and (d) DMAPA-treated devices.

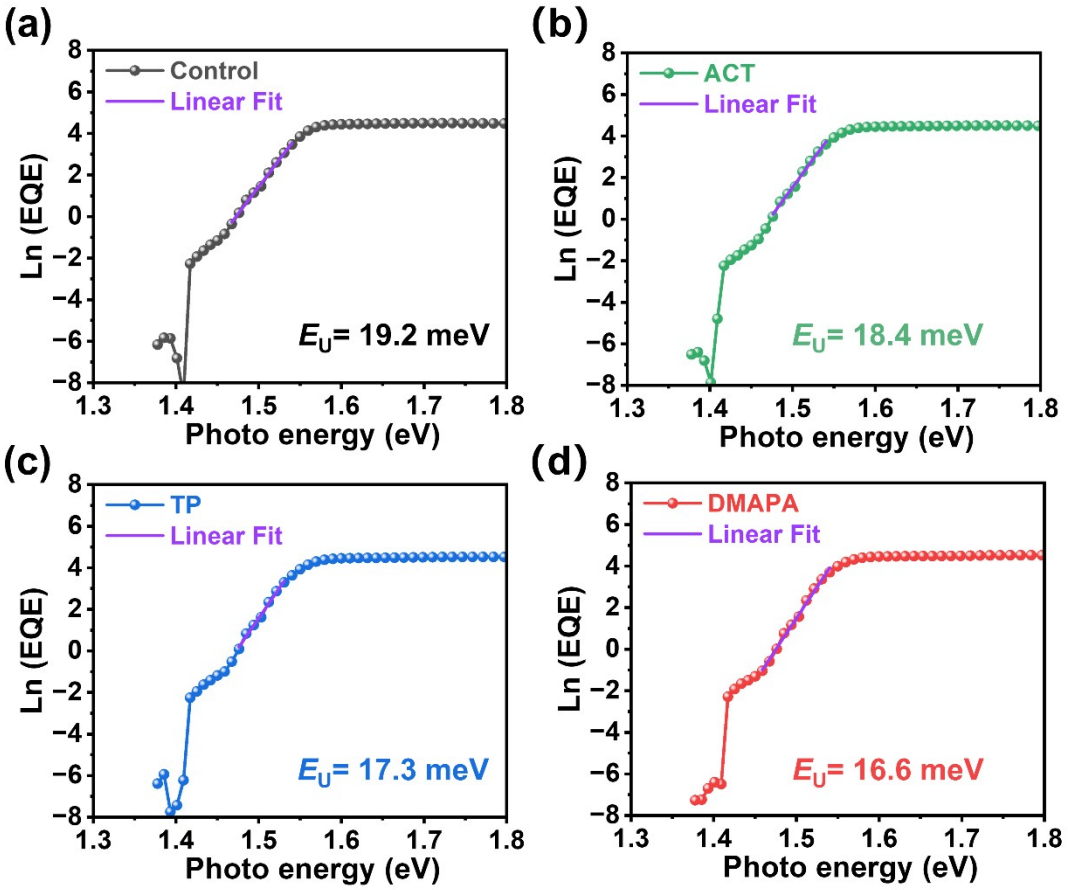

Figure S14. The estimation of E_U for (a) control, (b) ACT-, (c) TP-, and (d) DMAPA-treated devices.

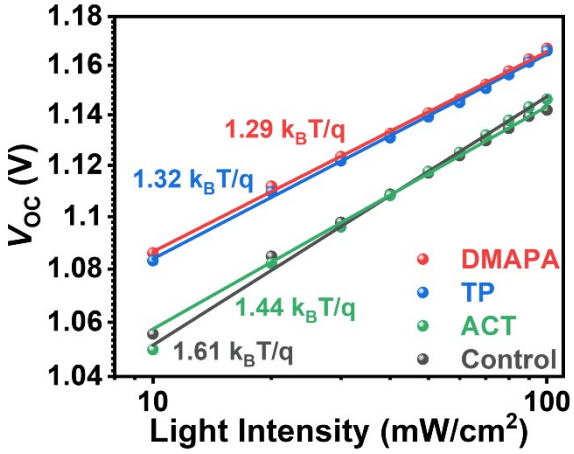

Figure S15. J_{SC} dependence upon light intensity of the control and different ligand-based devices.

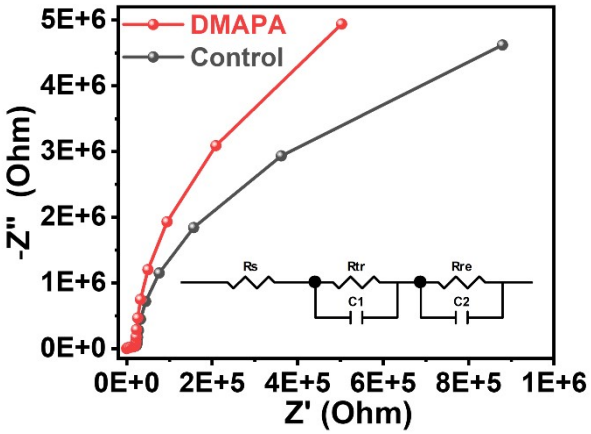

Figure S16. EIS plots for the of the control and DMAAP-based device. The inset is the equivalent circuit model.

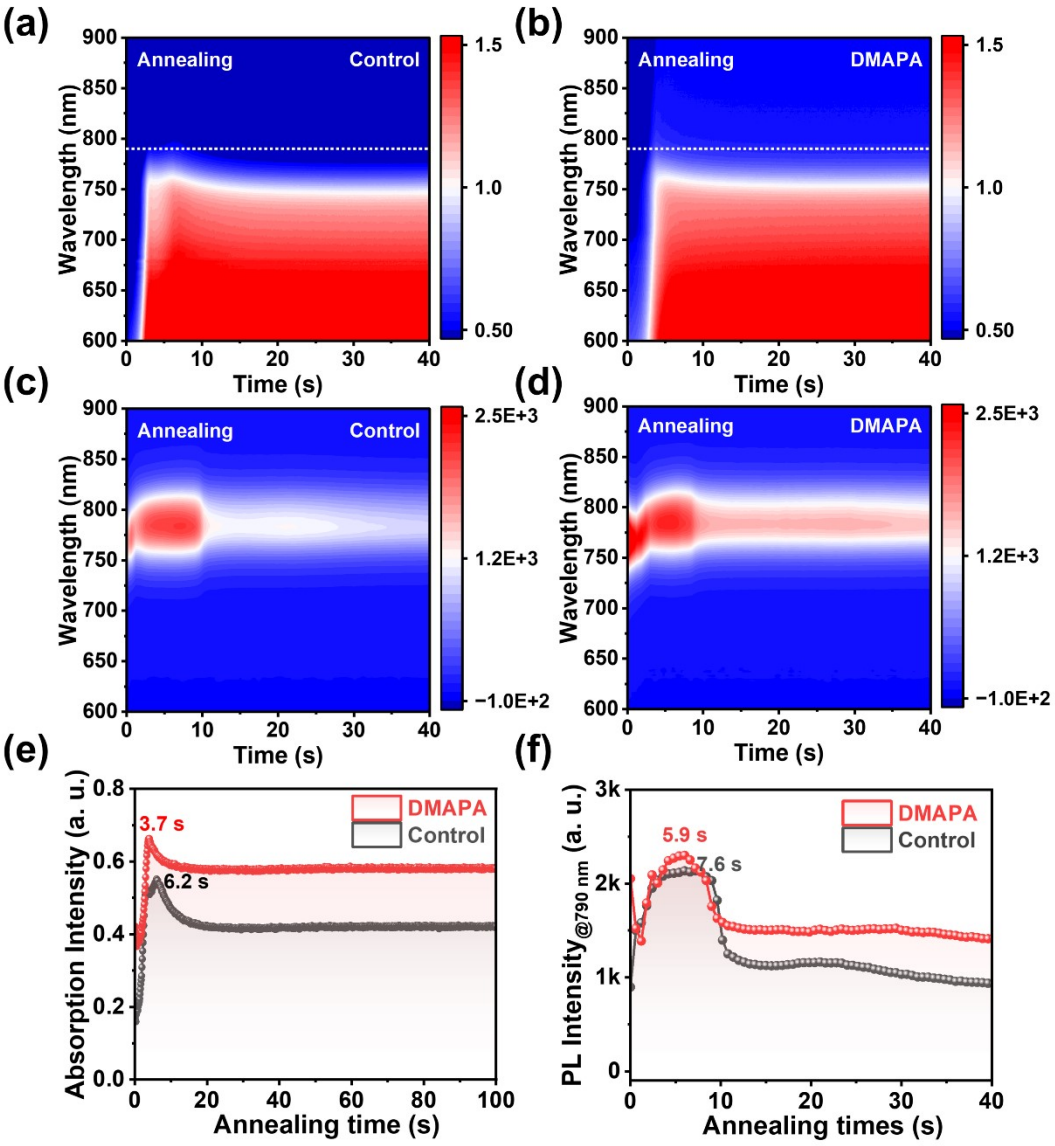

Figure S17. In-situ UV-vis spectra of (a) the control and (b) DMAPA-based perovskite films during the annealing process. In-situ PL spectra of (c) the control and (d) DMAPA-based perovskite films during the annealing process. Evolution of (e) absorption intensity and (f) PL intensity at 790 nm for perovskite films during the annealing process.

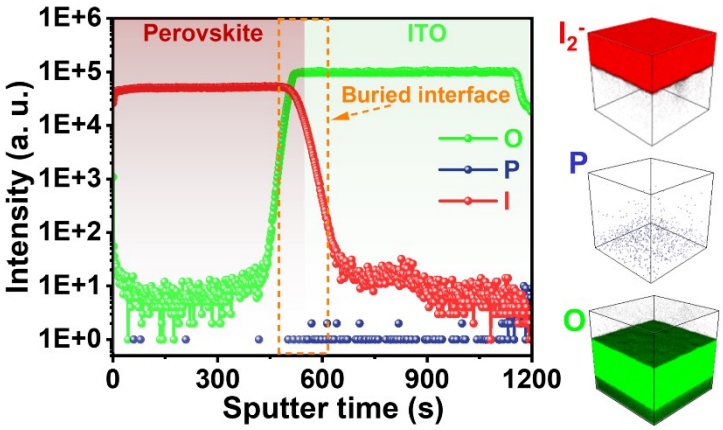

Figure S18. ToF-SIMS depth profiles and the corresponding spatial distribution of O, I, and P element in the control films deposited directly on bare ITO substrate.

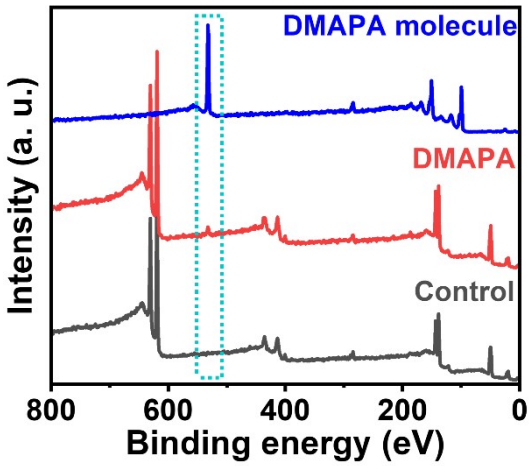

Figure S19. The survey XPS spectra of the control perovskite, DMAPA-based perovskite, and the pure DMAPA molecule.

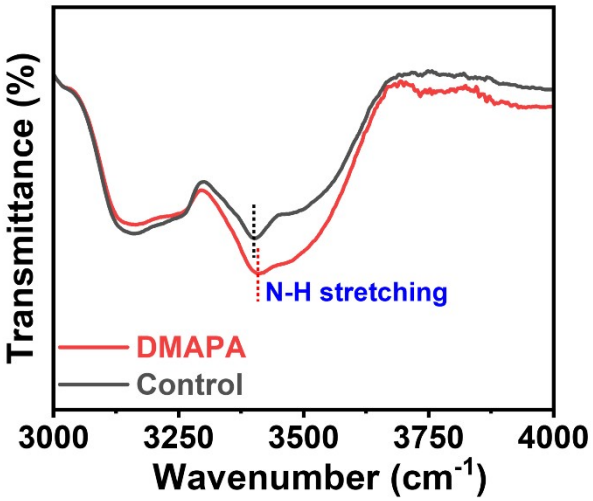

Figure S20. FTIR spectra in the wavenumber of 3000 to 4000 cm^{-1} for the control and DMAPA-based perovskite films.

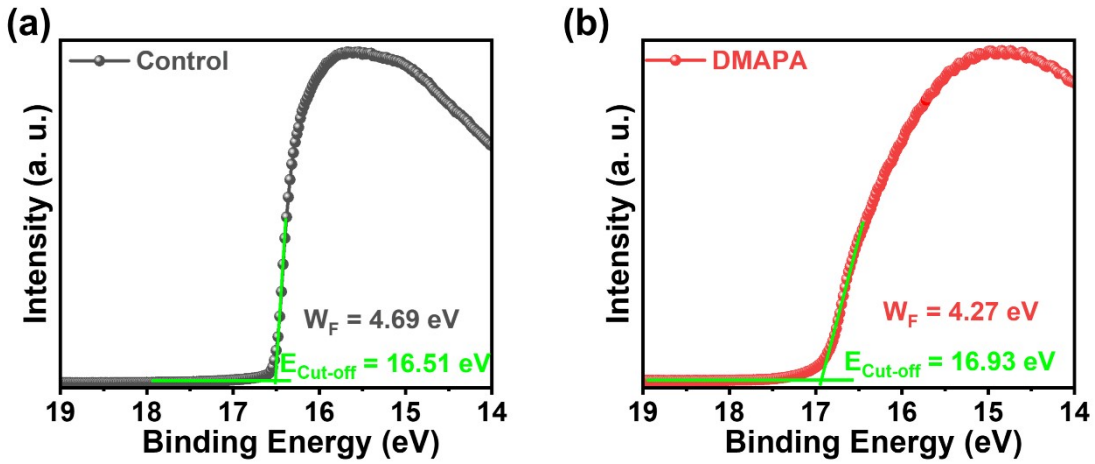

Figure S21. The secondary electron cut-off region of (a) the control and (b) DMAPA treated perovskite films.

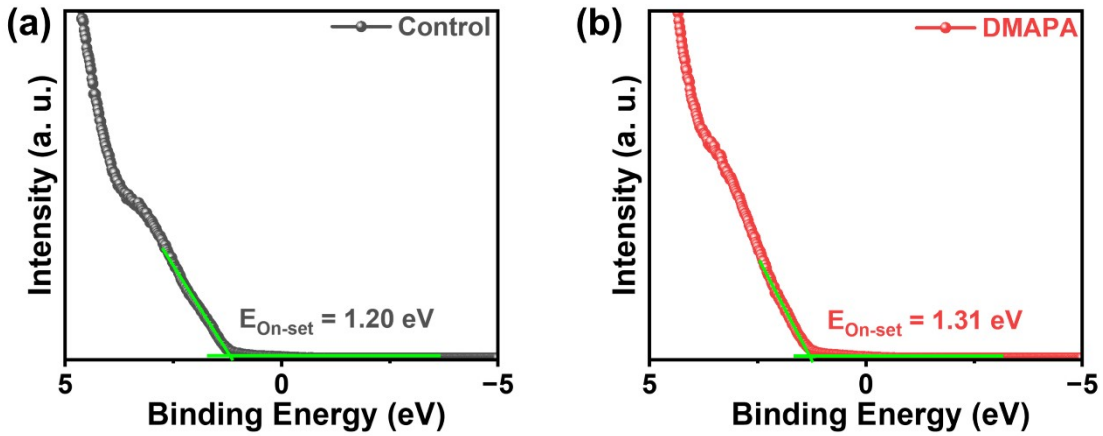

Figure S22. The valence band region of (a) the control and (b) DMAPA treated perovskite films.

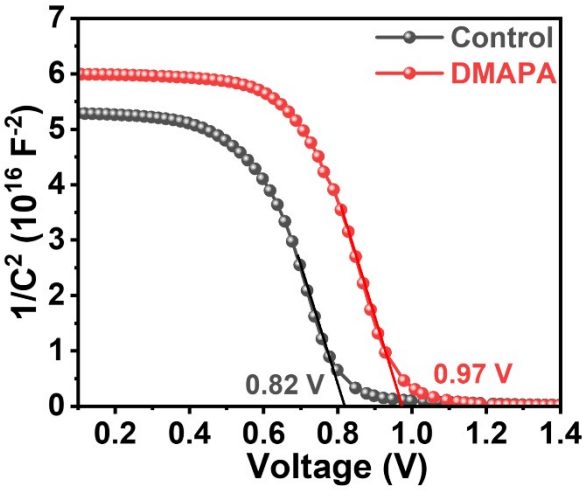

Figure S23. The Mott-Schottky plots for the control and DMAPA-based devices.

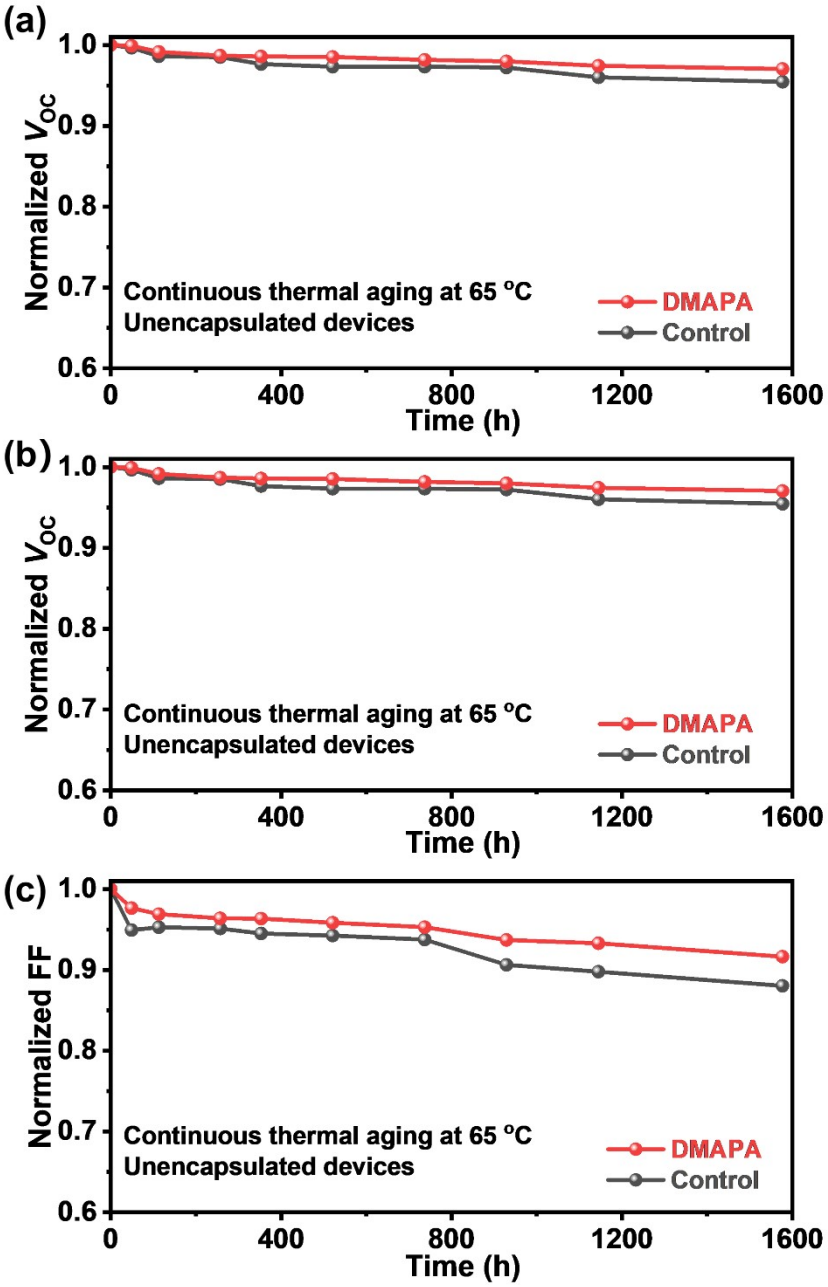

Figure S24. (a) V_{OC}, (b) J_{SC}, and (c) *FF* as functions of aging times in the thermal stability at 60 °C in nitrogen (N_2) atmosphere for unencapsulated PSCs.

Table S1. TRPL lifetimes of the control and treated perovskite films fitted from the decay curves by a biexponential model.

Substrate	A_1	τ_1 (ns)	A_2	τ_2 (ns)	τ_{ave} (ns)
Control	0.44	28.41	0.43	3393.90	3364.87
ACT	0.32	66.52	0.58	4704.44	4668.19
TP	0.30	101.82	0.64	5279.35	5232.91
DMAPA	0.33	120.91	0.75	6343.48	6292.60

Table S2. Detailed PV parameters for the control devices.

Device	V_{OC} (V)	*FF* (%)	J_{SC} (mA/cm^2)	PCE (%)
1	1.13	77.58	24.94	21.88
2	1.13	79.70	24.52	22.08
3	1.12	78.05	25.22	22.08
4	1.13	79.24	24.85	22.22
5	1.13	78.85	24.69	21.97
6	1.14	78.70	24.64	22.12
7	1.13	78.51	24.99	22.15
8	1.13	77.28	25.26	22.01
9	1.14	79.74	24.92	22.67
10	1.14	78.96	24.93	22.53
11	1.14	78.48	24.73	22.21
12	1.13	79.93	24.97	22.56
13	1.12	77.47	25.07	21.84
14	1.15	77.44	24.81	22.00
15	1.14	79.26	25.29	22.87
16	1.13	78.48	24.73	21.99
17	1.13	78.96	24.62	22.06
18	1.13	77.75	25.06	22.08
19	1.13	79.61	24.90	22.41
20	1.13	79.24	24.85	22.22

Table S3. Detailed PV parameters for the ACT-based devices.

Device	V_{OC} (V)	*FF* (%)	J_{SC} (mA/cm^2)	PCE (%)
1	1.14	83.30	24.94	23.59
2	1.14	82.84	25.06	23.70
3	1.15	82.13	25.37	23.91
4	1.13	82.10	25.15	23.39
5	1.13	82.50	25.12	23.44
6	1.14	82.57	25.03	23.52
7	1.14	83.08	24.92	23.60
8	1.14	81.77	25.36	23.61
9	1.15	81.72	25.43	23.80
10	1.14	81.04	25.23	23.37
11	1.14	81.66	25.08	23.38
12	1.14	81.70	25.44	23.64
13	1.14	81.91	25.39	23.79
14	1.14	81.60	25.25	23.47
15	1.14	82.47	25.20	23.70
16	1.15	80.63	24.92	23.12
17	1.14	81.65	25.08	23.43
18	1.14	80.34	25.12	23.00
19	1.14	83.29	25.43	24.17
20	1.15	82.64	25.32	23.99

Table S4. Detailed PV parameters for the TP-based devices.

Device	V_{OC} (V)	*FF* (%)	J_{SC} (mA/cm^2)	PCE (%)
1	1.15	83.29	25.72	24.71
2	1.15	82.93	25.37	24.23
3	1.15	82.66	25.43	24.15
4	1.16	83.62	25.51	24.75
5	1.16	83.00	25.56	24.54
6	1.15	82.74	25.41	24.18
7	1.15	82.69	25.73	24.50
8	1.15	83.19	25.52	24.40
9	1.15	82.60	25.73	24.48
10	1.16	83.70	25.57	24.77
11	1.16	83.66	25.57	24.77
12	1.16	82.41	25.38	24.22
13	1.15	83.95	25.55	24.63
14	1.15	82.29	25.55	24.23
15	1.15	83.34	25.40	24.40
16	1.15	83.60	25.47	24.46
17	1.15	83.67	25.50	24.61
18	1.15	83.85	25.43	24.59
19	1.15	83.33	25.26	24.18
20	1.14	83.59	25.40	24.28

Table S5. Detailed PV parameters for the devices modified by ACT and TP mixture.

Device	V_{OC} (V)	*FF* (%)	J_{SC} (mA/cm^2)	PCE (%)
1	1.15	83.38	25.62	24.52
2	1.15	83.85	25.86	25.01
3	1.15	82.44	25.71	24.45
4	1.15	83.19	25.79	24.60
5	1.16	84.35	25.05	24.46
6	1.15	84.22	25.83	25.02
7	1.16	82.58	25.59	24.43
8	1.15	82.80	25.60	24.38
9	1.15	84.23	25.81	25.06
10	1.15	82.70	25.59	24.44
11	1.15	84.62	25.43	24.82
12	1.15	82.06	25.85	24.47
13	1.15	83.83	25.59	24.72
14	1.16	83.29	25.66	24.88
15	1.16	84.04	25.81	25.11
16	1.15	84.22	25.86	25.03
17	1.16	84.16	25.75	25.03
18	1.15	84.70	25.66	25.07
19	1.15	84.44	25.79	25.09
20	1.16	84.34	25.65	25.02

Table S6. Detailed PV parameters for the DMAPA-based devices.

Device	V_{OC} (V)	*FF* (%)	J_{SC} (mA/cm^2)	PCE (%)
1	1.18	83.34	25.70	25.19
2	1.17	83.59	25.60	25.12
3	1.17	83.58	25.82	25.24
4	1.17	83.93	25.81	25.38
5	1.17	83.33	25.70	25.02
6	1.17	83.86	25.55	25.01
7	1.18	83.25	25.54	24.99
8	1.18	84.04	25.75	25.45
9	1.17	84.04	25.75	25.42
10	1.17	83.63	25.84	25.28
11	1.17	83.70	25.69	25.19
12	1.17	83.42	25.67	24.98
13	1.17	83.52	25.80	25.21
14	1.16	84.44	25.58	25.12
15	1.17	83.78	25.78	25.30
16	1.17	83.84	25.81	25.35
17	1.17	83.92	25.87	25.40
18	1.17	84.64	25.86	25.59
19	1.17	83.07	25.63	24.94
20	1.17	83.47	25.71	25.01

Table S7. Photovoltaic parameters for the best-performing control and ligand-based devices in Figure 3d.

	J_{SC} (mA/cm^2)	V_{OC} (V)	*FF* (%)	PCE (%)	HI (%)
Control-Reverse	25.28	1.14	79.26	22.87	1.60
Control-Forward	25.17	1.14	78.57	22.50	
ACT-Reverse	25.37	1.15	82.13	23.91	1.39
ACT-Forward	25.09	1.14	82.26	23.57	
TP-Reverse	25.57	1.16	83.66	24.77	1.36
TP-Forward	25.80	1.15	82.47	24.43	
DMAPA-Reverse	25.86	1.17	84.64	25.59	0.72
DMAPA-Forward	25.93	1.17	83.81	25.40	

HI (Hysteresis index) = $(PCE_{Reverse} - PCE_{Forward})/PCE_{Reverse} \times 100\%$

Table S8. EIS parameters of the control and DMAPA-based devices in Figure S16.

	R_s (Ohm)	R_{tr} (Ohm)	C_1 (F)	R_{rec} (Ohm)	C_2 (F)
Control	20.13	24615	6.44E-09	2.58E+07	1.29E-08
DMAPA	7.82	21500	6.74E-09	5.12E+07	1.24E-08

References:

1. G. Kresse and D. Joubert, *Phys. Rev. B*, 1999, **59**, 1758-1775.
2. J. P. Perdew, K. Burke and M. Ernzerhof, *Phys. Rev. Lett.*, 1996, **77**, 3865-3868.